

CONF-821049--18

DE83 008694

Threshold Energy Surface and Frenkel-Pair Resistivity for Cu*

Wayne E. King and K. L. Merkle

Argonne National Laboratory, Argonne, IL 60439

M. Meshii

Northwestern University, Evanston, IL 60201

The submitted manuscript has been authored by a contractor of the U. S. Government under contract No. W-31-109-ENG-38. Accordingly, the U. S. Government retains a nonexclusive, royalty-free license to publish or reproduce the published form of this contribution, or allow others to do so, for U. S. Government purposes.

DISCLAIMER

This report was prepared as an account of work sponsored by an agency of the United States Government. Neither the United States Government nor any agency thereof, nor any of their employees, makes any warranty, express or implied, or assumes any legal liability or responsibility for the accuracy, completeness, or usefulness of any information, apparatus, product, or process disclosed, or represents that its use would not *infringe* privately owned rights. Reference herein to any specific commercial product, process, or service by trade name, trademark, manufacturer, or otherwise does not necessarily constitute or imply its endorsement, recommendation, or favoring by the United States Government or any agency thereof. The views and opinions of authors expressed herein do not necessarily state or reflect those of the United States Government or any agency thereof.

*Work supported by the National Science Foundation and the U.S. Department of Energy.

MASTER

eb
DISTRIBUTION OF THIS DOCUMENT IS UNLIMITED

Threshold Energy Surface and Frenkel Pair Resistivity for Cu*

Wayne E. King and K. L. Merkle

Argonne National Laboratory, Argonne, IL 60439

M. Meshii

Northwestern University, Evanston, IL 60201

Abstract

In-situ electrical resistivity damage-rate measurements in the high voltage electron microscope have been used to study electron-irradiation-induced defect production in copper single crystals at $T < 10$ K. Analysis of the directional and energy dependence yields a threshold energy surface that is significantly different from those of previous investigations: two pockets of low threshold energy centered at $\langle 100 \rangle$ and $\langle 110 \rangle$ surrounded by regions of much higher threshold energy. The corresponding damage function exhibits a plateau of 0.6 Frenkel pairs. The present results imply a Frenkel pair resistivity for Cu of $(2.75^{+0.6}_{-0.2}) \times 10^{-4} \Omega\text{-cm}$.

1. Introduction

Energetic neutrons, electrons and ions have been used in the past to simulate the radiation environment encountered by metals in nuclear reactors. The violent collision of these particles with lattice atoms can

*Work supported by the National Science Foundation and the U.S. Department of Energy.

initiate branching chains of atomic displacements referred to as collision cascades. The defect structure of the cascade is characterized by a vacancy-rich core surrounded by an interstitial cloud. One of the basic quantities one needs to know for predicting radiation effects is the number of point defects produced per cascade. Historically, the Kinchin-Pease (KP)¹ or modified Kinchin-Pease (MKP)² models have been relied on to predict the number of point defects, ν , created as a function of lattice atom recoil energy T . The KP model based on hard sphere collisions, is given by

$$\nu(T) = \begin{cases} 0 & \text{for } T < T_d \\ 1 & \text{for } T_d \leq T \leq 2T_d, \\ \frac{T}{2T_d} & \text{for } T \geq 2T_d \end{cases} \quad (1.11)$$

and the MKP model² is given by

$$\nu(T) = \begin{cases} 0 & \text{for } T < T_d \\ 1 & \text{for } T_d \leq T \leq 2.5 T_d, \\ \frac{0.8}{2T_d} \epsilon(T) & \text{for } \epsilon > 2.5 T_d \end{cases} \quad (1.12)$$

where T_d is the so-called "effective" threshold energy and $\epsilon(T)$ is the damage energy (recoil energy corrected for electronic losses).²

It is known that these damage functions over-estimate the defect production by a factor of 2-3 at high recoil energy² and are also completely inadequate at energies near threshold. Clearly the detailed form of the

damage function is essential for accurate defect production calculations. In addition, the true damage function can also provide much needed information on fundamental defect production mechanisms. At present, a great deal of information is available on the minimum threshold energy for atomic displacement in a variety of materials. However, only a few attempts have been made to extract the actual form of the damage function in the critical low energy regime.

The primary experimental technique that has been used in the past to study the damage function has been electrical-resistivity damage-rate measurements on electron irradiated polycrystalline samples at helium temperature.³⁻⁶ In metals, the introduction of Frenkel defects by irradiation yields a change in resistivity, $\Delta\rho$, which is proportional to the Frenkel pair resistivity, ρ_F , to the concentration of irradiation induced Frenkel pairs. The initial electrical-resistivity damage rate, i.e., the damage rate for the undisturbed lattice of a polycrystalline target is given by

$$\left. \frac{d\Delta\rho}{d\phi} (E_1) \right|_0 = \rho_F \int_0^{T_m} \frac{d\sigma(E_1)}{dT} \nu(T) dT \quad (1.2)$$

where $\frac{d\sigma(E_1)}{dT}$ is the Mott differential scattering cross section,⁷ E_1 is the energy of the incident electron beam, T_m is the maximum transferred energy in a head-on collision, and ϕ is the electron dose. In order to extract $\nu(T)$ from Eq. (1.2), damage-rate measurements as a function of incident electron beam energy and a knowledge of the Frenkel-pair resistivity are

required. If ρ_F is unknown, the absolute Frenkel pair concentration cannot be determined from Eq. (1.2) and only the quantity $\rho_F v(T)$ can be found.⁸

An alternative, albeit more complicated approach has been used by a few investigators. In these experiments, the directional dependence of the threshold energy, i.e., the threshold energy surface was derived from the analysis of single-crystal damage-rate measurements as a function of incident electron beam direction and energy. The damage function in the single displacement regime can then be derived from the threshold energy surface. In addition, the threshold energy surface provides basic information on the interaction of atoms at distances smaller than the nearest-neighbor separations and on the mechanisms by which interstitials are separated from their vacancies.

The present work examines damage-rate data for copper that were obtained by in-situ electrical-resistivity damage-rate measurements in the high voltage electron microscope (HVEM)^{9,10} as reported in Ref. 11. In that paper, the analysis was carried out based on the assumption that the Frenkel-pair resistivity for copper was 2.0×10^{-4} Ω -cm, the generally accepted value. Here, we shall discuss the results and validity of a different approach that allows, under optimum conditions, the determination of the Frenkel pair resistivity as well as the threshold energy surface. Analysis of the results yields a threshold energy surface characterized by two pockets of low threshold energy centered at $\langle 100 \rangle$ and $\langle 110 \rangle$ (~ 19 - 35 eV) surrounded by regions of much higher threshold energy (> 35 eV); the corresponding damage function exhibits a plateau at ~ 0.6 Frenkel pairs.

2. Basic Principles

2.1 Threshold Energy Surface and Damage Function

The coordinate system that will be used when referring to the incident electron beam directions and lattice atom recoil directions is shown in Fig. 1. The upper case Greek letters (Θ, Φ), refer to polar and azimuthal angles measured with respect to the [001] pole while the lower-case Greek letters (θ, ϕ) refer to angles measured with respect to the incident beam direction. The subscript 1 refers to the incident electrons and the subscript 2 refers to the target atom. The direction of the incident electron beam is specified by polar angle Θ_1 and azimuthal angle Φ_1 . The incident electrons are scattered by angles (θ_1, ϕ_1) (not shown). As a result of a scattering event, the target atom recoils at angle (θ_2, ϕ_2) in the crystal directions specified by (Θ_2, Φ_2) . The angle, ϕ_2 , is the included angle defined by the intersection of the two great circles containing poles $(\frac{\pi}{2}, \Phi_1)$, (Θ_1, Φ_1) , and (Θ_1, Φ_1) , (Θ_2, Φ_2) .

The total cross section for Frenkel pair production is given by:

$$\sigma_d(\Theta_1, \Phi_1; E_1) = \int_0^{\pi/2} \int_0^{2\pi} \frac{d\sigma(\theta_2; E_1)}{d\theta_2} H[T(\theta_2) - T_d(\Theta_2, \Phi_2)] \frac{d\phi_2}{2\pi} d\theta_2 \quad (2.11)$$

where $\frac{d\sigma(\theta_2; E_1)}{d\theta_2}$ is related to the Mott differential scattering cross

section $\frac{d\sigma}{d\theta_1}$,⁷ and T , the recoil energy, is related to the scattering angle θ_2 by $T = T_m \cos^2(\theta_2)$. We assume that the directionally dependent damage function $v(\theta_2, \phi_2; T)$ has the form of a Heaviside step function [$H(x) = 0$ for $x < 0$ and $H(x) = 1$ for $x \geq 0$].

In the single displacement regime the damage function is given by the probability to produce a Frenkel pair per recoil for a spatially isotropic distribution of recoils of energy T and is therefore obtained from the threshold energy surface by

$$v(T) = \int_0^{2\pi} \int_0^{\pi/2} H[T - T_d(\theta_2, \phi_2)] \frac{\sin\theta_2}{4\pi} d\theta_2 d\phi_2. \quad (2.12)$$

The total cross section for Frenkel pair production is related to the initial damage rate via the Frenkel pair resistivity

$$\sigma_d(\theta_1, \phi_1; E_1) = \frac{1}{\rho_F} \left. \frac{d\Delta\rho}{d\phi} \right|_0(\theta_1, \phi_1; E_1) \quad (2.13)$$

2.2 Fitting the Threshold Energy Surface

The unit triangle was divided into 41 ($5^\circ \times 5^\circ$) regions. Each of these regions was assigned a first-guess threshold energy value based on the threshold surface of Ref. 11. The threshold energy surface and the Frenkel pair resistivity were determined via a derivative type, unconstrained optimization scheme.¹² This procedure minimizes the value of a goodness-of-fit parameter, χ^2 , by simultaneously optimizing all regions of the

threshold energy surface using a gradient technique. χ^2 is defined by

$$\chi^2 = \frac{1}{k-s} \sum_{i=1}^k \frac{(\sigma_i^{\text{obs}} - \sigma_i^{\text{calc}})^2}{W_i^2} \quad (2.21)$$

where σ_i^{obs} and σ_i^{calc} correspond to the observed and calculated total cross sections for Frenkel pair production, k is the number of experimental observations* s is the number of free parameters, i.e., the number of adjustable $5^\circ \times 5^\circ$ threshold energy regions plus ρ_F , and $k-s$ is referred to as the number of degrees of freedom. Equation (2.11) is solved using a set of routines (LMSTR, LMSTR1, and COVAR) from the MINIPACK-1¹³ package of FORTRAN language sub-programs for the solution of nonlinear equations and nonlinear least squares problems.

3. Experimental

Details regarding the HVEM helium cooled stage and specimen preparation may be found in Refs. 9-11. We shall concentrate in this section on those aspects of the experimental procedure that were not discussed in detail in Ref. 11.

3.1 Energy Calibration

The energy of the electron beam was measured at each energy that was used by recording a diffraction pattern from an aluminum polycrystalline

*In this work, 180 damage-rate measurements were carried out at five energies between 0.5 and 1.1 MeV in ~ 40 directions distributed over the unit stereographic triangle.

test specimen. The specimen was mounted in a special holder located below the final lens of the HVEM to eliminate uncertainties in the camera length, i.e., distance from the specimen to the photographic plate, introduced by the magnetic lenses. The diameters of the first five rings in the diffraction pattern were used to determine the average wavelength given by

$$\lambda = \frac{d_i D_i}{2L} \quad (3.11)$$

where D_i is the diameter of ring i , d_i is the interplanar spacing that corresponds to ring i , and L is the camera length. The electron energy was found by solving the following equation¹⁴

$$\lambda = \frac{12.236}{[E_1(1+0.9788 \times 10^{-6} E_1)]^{1/2}} \text{ \AA} \quad (3.12)$$

where E_1 is the electron energy in electron volts. Using this procedure, it was possible to determine the electron energy to within 1%.

3.3 Irradiations

The details of the irradiation are given in Ref. 11. The specimens were first aligned using Kikuchi patterns such that the [001] direction, which was perpendicular to the sample surface, was nearly parallel with the electron beam. This direction was referred to as the reference direction. The specimen was irradiated in this direction followed by alternating irradiations in a tilted direction and the reference direction. Four "tilt paths" were investigated, three on one specimen and one on another.

In this way, data from throughout the unit triangle were collected. Tests for reproducibility of the data and the effect of subthreshold annealing on the results are discussed in Ref. 11. Exact coincidence of the electron beam direction with low index crystallographic axes was avoided in order to minimize Bloch-wave channeling.¹⁵

3.4 Correction for the Electrical Resistivity Size Effect

The measured damage rates were corrected for the electrical-resistivity size effect using the Fuchs-Sondheimer theory.¹⁶ The probability of specular reflection of the conduction electrons at the specimen surface was taken to be zero and the ratio of the film thickness, a , to the mean-free path of the conduction electrons, λ , was chosen in a self-consistent manner. First, the damage rate vs radiation induced resistivity increment for the reference direction was fit with a polynomial. Damage rates for particular electron beam directions along a tilt path were normalized to the reference direction damage rate at the same value of irradiation induced electrical resistivity. This quotient is independent of the electrical-resistivity size effect. The raw data was then adjusted using a size effect parameter ($\gamma = a/\lambda$), corrected for the saturation effect, and normalized to the corrected reference direction initial damage rate. These corrected normalized damage rates were then compared to the uncorrected normalized rates and the size effect parameter was adjusted until an optimum mean-squared difference between the two sets of normalized damage rates was obtained. This is illustrated in Fig. 2

where the mean-square difference, R , is plotted as a function of size effect parameter γ for a scan at 0.900 MeV. This procedure was found to be very sensitive to the value of γ that was chosen.

4. Results

4.1 Threshold Energy Surface

The measured total cross sections for Frenkel pair production for the four scans discussed above are plotted in Ref. 11. Using this data, a solution to Eq. (2.11) was obtained by variationally optimizing the threshold energy surface as described in Section 2.2. Optimizations were carried out including ρ_F as a free parameter. This resulted in a χ^2 value of 1.06 and $\rho_F = 2.85 \times 10^{-4}$ Ω -cm. To study the uniqueness of this fit, optimizations were carried out as a function of the parameter ρ_F . The value of χ^2 is plotted as a function of ρ_F in Fig. 3.* The best fit threshold energy surface is shown in Fig. 4. The minimum threshold energy is 19 eV located near [100]. The spatial average threshold energy is ~ 41 eV. The best fit threshold energy surface of Fig. 4 is plotted in Fig. 4b as a three-dimensional plot of the unit triangle with the Z-axis corresponding to the threshold energy. This surface is characterized by two pockets of low threshold energy centered at $\langle 100 \rangle$ and $\langle 110 \rangle$ surrounded by regions of much

*This result indicates that the best-fit value of ρ_F is

$$(2.75 \pm 0.6) \times 10^{-4} \text{ } \Omega\text{-cm.}$$

higher threshold energy. This topography is in contrast to that of previously derived threshold energy surfaces which are generally of low threshold energy except in the vicinity of $\langle 111 \rangle$, e.g., see Ref. 11.

4.2 Damage Function

The damage function for Cu, $\nu(T)$, in the single displacement regime was determined by substituting the threshold energy surface of Fig. 4 into Eq. (2.12). Because most directions within the two regions around $\langle 100 \rangle$ and $\langle 110 \rangle$ become productive quite close to the minimum threshold energy, the resulting damage function shown in Fig. 5 exhibits a relatively sharp increase starting at the minimum threshold energy (~ 19 eV). This sharp onset is followed by a plateau at $\nu(T) \cong 0.6$ for $T \geq 35$ eV. The plateau reflects the sharp rise in threshold energy at the boundary between the low and high threshold energy regions (Fig. 4). Because of the insensitivity of electron irradiation damage experiments to the high threshold energy regions, the extent of this plateau could not be accurately determined. The molecular dynamics simulation of King et al.¹⁷ indicate that the plateau could extend to as high as ~ 125 eV. The existence of this plateau which has recently been confirmed in polycrystalline irradiations,¹⁸ means that simple damage functions like KP^1 and MKP^2 cannot be expected to accurately predict defect production for recoils near to the threshold energy. It also indicates that the average threshold energy for Cu is quite high. The average threshold energy as determined from Fig. 5 is

~ 41 eV. However, because of the uncertainties in the high energy threshold regions, this value has to be viewed with considerable caution. It is easily seen that if the energy T at which $v(T)$ reaches a value of one is increased by a factor of two, the corresponding increase in the average threshold energy could be of the same order. King et al. find a value for the average threshold energy of ~ 100 eV as deduced from molecular dynamics simulations.¹⁷

5. Discussion

5.1 Topographical Comparisons

In this presentation, we restrict our discussion to comparisons with previous investigations that have developed threshold energy surfaces for Cu, i.e., the works of King and Benedek,¹⁹ King et al.,¹¹ Schwartz et al.,²⁰ and Jung et al.²¹ (The pioneering work of Gibson et al.²² has been omitted in light of recent more extensive calculations of King and Benedek.¹⁹) A summary of other investigations on copper can be found in Ref. 11.

King and Benedek¹⁹ used a modified version of the molecular dynamics simulation code SUPERGLOB to study the directional dependence of the threshold energy. The Gibson II¹⁹ interatomic potential was used to model the atomic interactions. In order to compare this result with the present work, the unit triangle has been divided into 41 ($5^\circ \times 5^\circ$) regions and the threshold energy value of each region was obtained by interpolation from the results of King and Benedek.¹⁹ The topography of this surface can be

found in Ref. 19 or 23. This surface has basically the same topographical characteristics as that of Fig. 4. The minimum threshold energy is ~ 25 eV and is located slightly off of $\langle 100 \rangle$ and $\langle 110 \rangle$. A ridge of high threshold energy between $\langle 100 \rangle$ and $\langle 110 \rangle$, similar to that shown in Fig. 4 is also observed in the simulated threshold energy surface between $\langle 100 \rangle$ and $\langle 110 \rangle$. Maxima in the threshold energy (> 100 eV) are observed to exist between $\langle 100 \rangle$ and $\langle 111 \rangle$ and between $\langle 110 \rangle$ and $\langle 111 \rangle$. A local minimum exists around $\langle 111 \rangle$. A peak in the threshold-energy surface is observed near the center of the unit triangle.

The surface of King et al.¹¹, Fig. 6a is generally of low threshold energy ($\sim 80\%$ of the surface is < 35 eV) with a small region of high threshold energy (> 45 eV) in the vicinity of $\langle 111 \rangle$.

Schwartz et al.²⁰ used the quasidynamic computer codes ADDES with the Molière approximation to the Thomas-Fermi screening function to describe the atomic interactions to determine threshold energies for 20 directions distributed over the unit triangle. Their threshold energy surface is shown in Fig. 6 [again obtained by interpolation and divided into 41 ($5^\circ \times 5^\circ$) blocks]. The minima in the threshold energy surface are located in the vicinity of $\langle 100 \rangle$ and $\langle 110 \rangle$. A ridge is also observed to separate $\langle 100 \rangle$ and $\langle 110 \rangle$. A local minimum is observed near $\langle 111 \rangle$.

Jung et al.²¹ electron irradiated single-crystal specimens as a function of energy (5 energies between 1.13 and 1.89 MeV) and direction (around the perimeter of the unit triangle). The threshold energy surface was deduced from a computer fit to ~ 40 normalized damage rates using ~ 40

adjustable parameters. The limits of the threshold energy surface deduced in that work are shown in Fig. 6c and 6d. The minimum threshold energy resides near $\langle 100 \rangle$ and $\langle 110 \rangle$.

Each of the surfaces described above exhibit minima in the threshold energy near the close-packed directions $\langle 100 \rangle$ and $\langle 110 \rangle$. Further, they all show a marked increase in the vicinity of $\langle 111 \rangle$. However, a clear difference exists among these threshold energy surfaces when comparing the region halfway between $\langle 100 \rangle$ and $\langle 110 \rangle$. It is observed that in the present surface (Fig. 4) a ridge of high threshold energy effectively separates the low threshold energy regions surrounding $\langle 100 \rangle$ and $\langle 110 \rangle$ from each other. This ridge is also observed in the surface of King and Benedek¹⁹ and in the work of Schwartz et al.²⁰ (Fig. 6b) but not in the other surfaces. King and Benedek²³ have shown that the presence of this ridge is a necessary consequence of the branching²⁴ mechanism.*

5.2 Quantitative Comparisons

Measured total cross sections for Frenkel pair production ($\rho_F = 2.75 \times 10^{-4}$ Ω -cm) as a function of incident electron beam energy and direction were compared with those calculated from the threshold energy surfaces of Fig. 4, 7a-d and the surface of King and Benedek.¹⁹ The

*Recently we have reanalyzed the experimental results of Jung et al.²¹ and have derived a threshold energy surface. Although we have neglected the effect of multiple scattering on Jung's data, the surface that was derived also exhibited a pronounced ridge half-way between $\langle 100 \rangle$ and $\langle 110 \rangle$.

present surface is observed to fit the experimental data to within $\sim 10\%$ over all energies and directions. This is easily observed when the measured total cross sections for Frenkel-pair production are plotted along with the calculated total cross sections in Fig. 7a-p. The exact beam directions are shown in the unit triangle in the upper left of each panel. The cross-hatched areas indicate the range of cross sections predicted by the surface of Jung et al.²¹ The solid line corresponds to the cross sections predicted by the present threshold energy surface. The error bars on the experimental points are the same as those used in Ref. 11. It is observed that both the surface of King and Benedek¹⁹ and Schwartz et al.²⁰ consistently underestimate the total cross section for Frenkel pair production. It is reasonable that these threshold energy surfaces do not fit the data exactly due to the manner in which the interatomic potentials were selected. On the other hand, both measurement and calculation lie below the prediction of the threshold energy surfaces of Jung et al.²¹ and King et al.¹¹ This difference can be accounted for, at least in part, by the increase in ρ_F in the present work.*

5.3 Characteristics of the Threshold Energy Surface

Some questions arise when we compare the topography of the threshold energy surface of Ref. 11 and the present work. Clearly, the primary

*Our reanalysis of the data of Jung et al.,²⁰ mentioned earlier, indicated that a value of ρ_F that was higher than the value derived by Jung et al.²⁰ gave the best fit to their data.

difference is the marked growth of the ridge of high threshold energy separating $\langle 100 \rangle$ and $\langle 110 \rangle$. This region is indicated in Fig. 8a. How is it possible that fitting two threshold energy surfaces to the same set of damage-rate data using two different Frenkel pair resistivities gives rise to such a large change only in this rather small ridge region as opposed to e.g. a small uniform increase in the threshold energy over the entire unit triangle? In the present optimization procedure, once an optimum fit is obtained, changes in the threshold energy of any region of the threshold energy surface will degrade the goodness-of-fit, i.e., yield a higher value of χ^2 . For example, let us explore the critical ridge region by investigating how changes in the threshold energy of the ridge region influences χ^2 . To do this, we begin with the threshold energy surface corresponding to Ref. 11 and increase the threshold energy in the ridge region by scaling factors from 1.0 to 1.4. The increase in χ^2 shown in Fig. 8b, with scaling factor indicates that for this surface, a ridge in the threshold energy surface does not produce an optimum fit to the experimental data. Refer now to Fig. 8c, where a similar plot is drawn for the present threshold energy surface, but in this case, the ridge was decreased. The strong increase in χ^2 as the height of the ridge was lowered, while all other threshold energies are held constant, indicates how sensitive the goodness-of-fit is to changes in this very important ridge region and that this high ridge is required for an optimum fit to the experimental data.

One might hypothesize that since the the increase in ρ_F from $2.0 \times 10^{-4} \Omega\text{-cm}$ to $2.75 \times 10^{-4} \Omega\text{-cm}$ effectively decreases the measured total

cross section for Frenkel-pair production [from Eq. (2.13)], a corresponding increase in the threshold energy over the entire unit triangle would compensate and yield an equally good fit to the experimental data as the present proposed surface. To show that this is not the case, we begin with the threshold energy surface corresponding to Ref. 11 (in which the ridge is absent), took the best-fit value of $\rho_F = 2.75 \times 10^{-4}$ Ω -cm and determined χ^2 as a function of a scaling factor for the entire threshold-energy surface, i.e., each threshold-energy region was scaled by a constant and the resulting χ^2 value was plotted as a function of the scaling factor. The result is shown in Fig. 9. The corresponding values of $\chi^2 \geq 5.0$ means that the calculated damage rates agree with the measured damage rates to within only 50%. This is significantly worse than the goodness-of-fit for the present best-fit surface where the calculated damage rates agree with the measured damage rates to within 10% over all energies and directions. Thus we cannot obtain the same goodness-of-fit by slight overall enhancement of the threshold-energy surface.

5.4 Validity of the Step Function Assumption

Molecular dynamics simulations by Schiffgens and Bourquin²⁵ have shown that for certain PKA directions, $v(\theta_2, \phi_2; T) = 0$ for certain energies, $T > T_d(\theta_2, \phi_2)$, in direct contradiction to our assumption that $v(\theta_2, \phi_2; T)$ has the form of a Heaviside-step function. Clearly, if nonmonotonic behavior is observed throughout the unit triangle, the analysis of single-crystal damage rate data as we have described is invalid. King and

Benedit¹⁹ have studied the pervasiveness of this phenomenon in detail. They have shown that this effect is restricted to directions where branching plays an important role in the defect production process, i.e., the high threshold energy directions. The step function assumption was however well satisfied in the regions of low threshold energy. Because the high threshold energy regions contribute very little to defect production in the present experiment, the breakdown of the Heaviside step-function assumption is not expected to strongly influence the results. One important point is that the damage function can be established from single crystal experiments only for those regions where the assumption holds. Single crystal experiments, however, are no less important since the initial portion of the damage function and the Frenkel-pair resistivity (which is essential for damage-function determinations via polycrystal experiments) can be determined.

6. Summary

The electron damage rate measurements reported earlier were reanalyzed allowing the Frenkel-pair resistivity to be a free parameter. The resulting threshold-energy surface is characterized by two pockets of low-threshold energy (19-35 eV) centered at $\langle 100 \rangle$ and $\langle 110 \rangle$ surrounded by regions of very high threshold energy. Although this surface is significantly different than those proposed in the past, the topology is observed to be in good agreement with that of molecular dynamics computer simulation

and is supported by a simple model for defect production. The corresponding damage function has a sharp step at the minimum threshold energy (~ 19 eV) followed by a plateau of 0.6 Frenkel pairs for $T > 30$ eV. These results have been recently confirmed by polycrystal irradiations described in this volume by Merkle et al.²⁶ Our best estimate of ρ_F is $(2.75 \pm \begin{smallmatrix} 0.6 \\ 0.2 \end{smallmatrix}) \Omega\text{-cm}$.

Acknowledgements

The authors gratefully acknowledge the valuable suggestions of and discussions with Dr. R. Benedek. Thanks are also due to Dr. O. S. Oen for calculating the ratio of Mott to Rutherford scattering in our energy regime. This work has been supported by the Metallurgy Program, Metallurgy and Materials Section, Division of Materials Research, National Science Foundation, Washington, D.C. under Grant DMR-8114845 and by the U.S. Department of Energy.

References

1. G. H. Kinchin and R. S. Pease, Rep. Prog. Phys. 18, 1 (1955).
2. R. S. Averback, R. Benedek, and K. L. Merkle, Phys. Rev. B18, 4156 (1978) and J. Nucl. Mater. 75, 162 (1978).
3. J. Wurm Report KFA Jülich Jül-581-FN March 1969.
4. G. W. Iseler, H. I. Dawson, A. S. Mehner, and J. W. Kaufmann, Phys. Rev. 146, 468 (1966).
5. P. Jung, B. R. Nielsen, H. H. Andersen, J. F. Bak, H. Knudsen, R. R. Coltman, Jr., C. E. Klabunde, J. M. Williams, M. W. Guinan, and C. E. Violet, Effects of Radiation on Materials: Eleventh Conference, ASTM STP 782, H. R. Brager and J. S. Perrin, Eds., American Society for Testing and Materials, 1982, pp. 963-982.
6. P. Jung, Phys. Rev. B 23, 664 (1981).
7. O. S. Oen (private communication) and in "Cross Sections for Atomic Displacement in Solids by Fast Electrons," Oak Ridge National Laboratory Report No. 4897, 1973.
8. H. J. Wollenberger in Vacancies and Interstitials in Metals (North-Holland, Amsterdam, 1969), pp. 215-254.
9. Wayne E. King, K. L. Merkle, and M. Meshii in Electron Microscopy 1980, High Voltage, Vol. 4, edited by P. Brederoo and J. Van Landuyt, Seventh European Congress on Electron Microscopy Foundation, Leiden, The Netherlands, 1980, 330-333.
10. Wayne E. King, K. L. Merkle, and M. Meshii, in Advanced and Alternate Techniques for Characterization of Microstructures, edited by F. W.

- Wiffen and J. A. Spitznagle (in press).
11. Wayne E. King, K. L. Merkle, and M. Meshii, Phys. Rev. B23, 6319 (1981).
 12. Jorge J. Moré in Lecture Notes in Mathematics (Springer, Berlin, 1978), pp. 105-116.
 13. Jorge J. Moré, Burton S. Garbon, Kenneth E. Hillstrom, User Guide for MINIPACK-1, Argonne National Laboratory Report No. ANL-80-74 (1980).
 14. K. W. Andrews, D. J. Dyson and S. R. Keown in Interpretation of Electron Diffraction Patterns, (Hilger, London, 1971), p. 5.
 15. L. E. Thomas, Radia. Eff. 5, 183 (1970).
 16. E. H. Sondheimer, Adv. Phys. 1, 1 (1952).
 17. Wayne E. King, R. Benedek, K. L. Merkle, and M. Meshii, Proceedings of the Yamada Conference V on Point Defects and Defect Interactions in Metals (1981), Kyoto, in press.
 18. K. L. Merkle, Wayne E. King, G. C. Baily, K. Haga, and M. Meshii, these proceedings.
 19. Wayne E. King and R. Benedek, Phys. Rev. B23, (1981).
 20. D. M. Schwartz, R. G. Ariyasu, J. O. Schiffgens, D. G. Doran, and G. R. Odette in proceedings of the 1976 International Conference on Computer Simulation for Materials Applications, Gaithersburg, Maryland, April 1976 (National Bureau of Standards, Washington, D.C., 1976), pp. 75-88.
 21. P. Jung, R. L. Chaplin, H. J. Fenzl, K. Reichelt, and P. Wombacher, Phys. Rev. B8, 553 (1973).

22. J. B. Gibson, A. N. Goland, M. Milgram, and G. H. Vineyard, Phys. Rev. 120, 1229 (1960).
23. Wayne E. King and R. Benedek, these proceedings.
24. P. Lucasson and A. Lucasson, Radia. Eff. 39, 195 (1978).
25. J. O. Schiffgens and R. D. Bourquin, J. Nucl. Mater. 69&70, 790 (1978).
26. K. L. Merkle, Wayne E. King, A. C. Baily, K. Haga, and M. Meshii, these proceedings.

Figure Captions

Fig. 1. The coordinate system used in this development showing the incident electron beam direction (θ_1, ϕ_1) and the recoil direction of the lattice atom (θ_2, ϕ_2) .

Fig. 2. Mean squared difference between size effect corrected and uncorrected normalized damage rates as a function of the ratio of the film thickness a to the electron mean free path λ .

Fig. 3. Chi-squared as a function of ρ_F .

Fig. 4a. Best-fit threshold energy surface corresponding to $\rho_F = 2.85 \times 10^{-4} \text{ } \Omega\text{cm}$.

Fig. 4b. Four orthogonal views of three-dimensional plots of Fig. 4a with z-axis corresponding to the threshold energy.

Fig. 5. Damage function derived from the best-fit threshold energy surface of Fig. 4.

Fig. 6. Three dimensional plots of the threshold energy surfaces of (a) King et al.,¹¹ (b) Schwartz et al.,²⁰ and (c and d) Jung et al.²¹ (c and d correspond to the limits given by Jung et al.²¹).

Fig. 7. Total cross sections as a function of incident beam direction for the directions shown in the inset unit triangle for the energies shown at top left.

Fig. 8a. Unit stereographic triangle showing the ridge region.

Fig. 8b. χ^2 as a function of the height of the ridge region between $\langle 100 \rangle$ and $\langle 110 \rangle$ for the threshold energy surface of Ref. 11.

Fig. 8c. χ^2 as a function of the height of the ridge region between $\langle 100 \rangle$ and $\langle 110 \rangle$ for the present threshold energy surface.

Fig. 9. χ^2 as a function of scaling factor for the entire threshold energy surface.

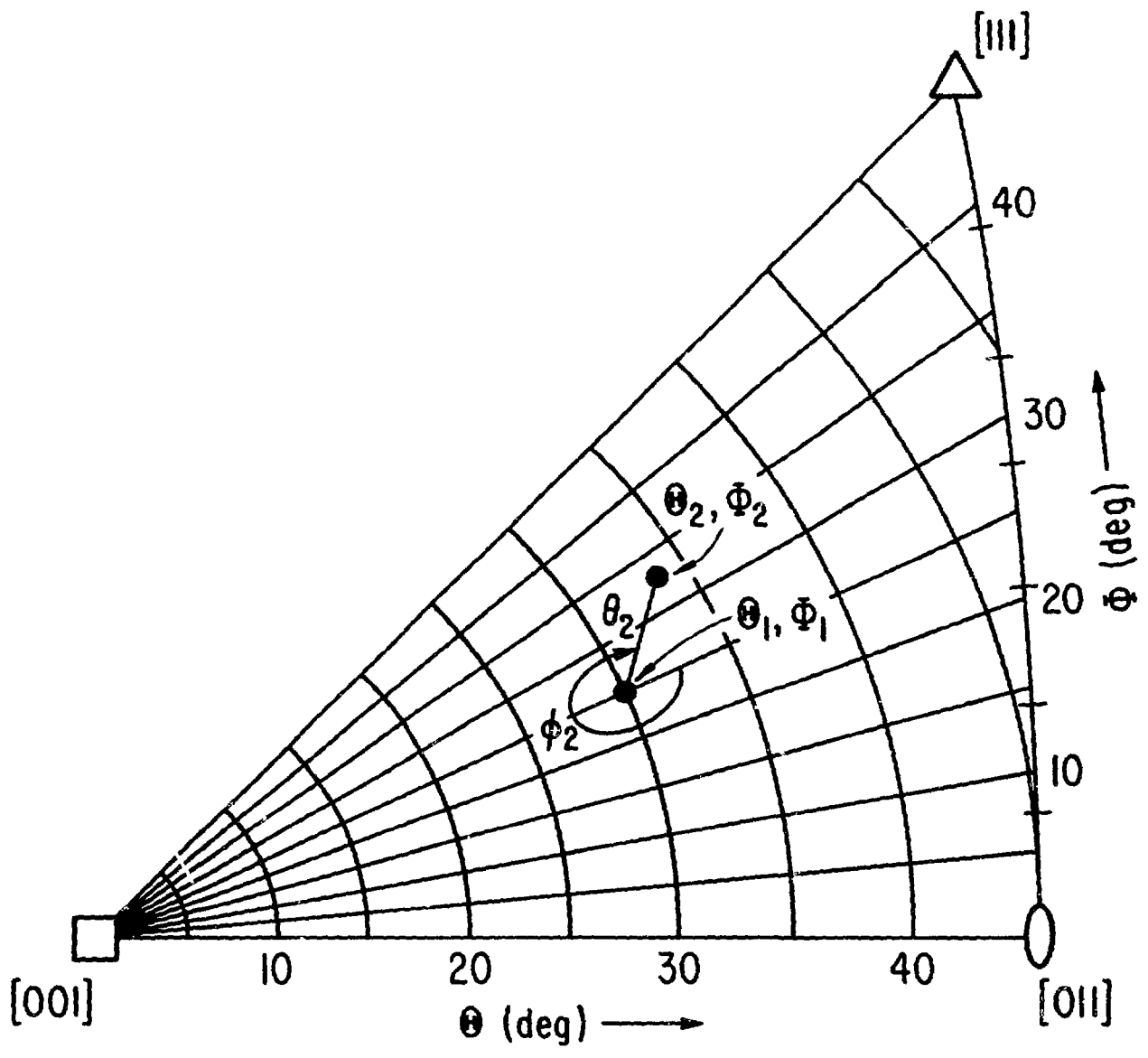


Figure 1

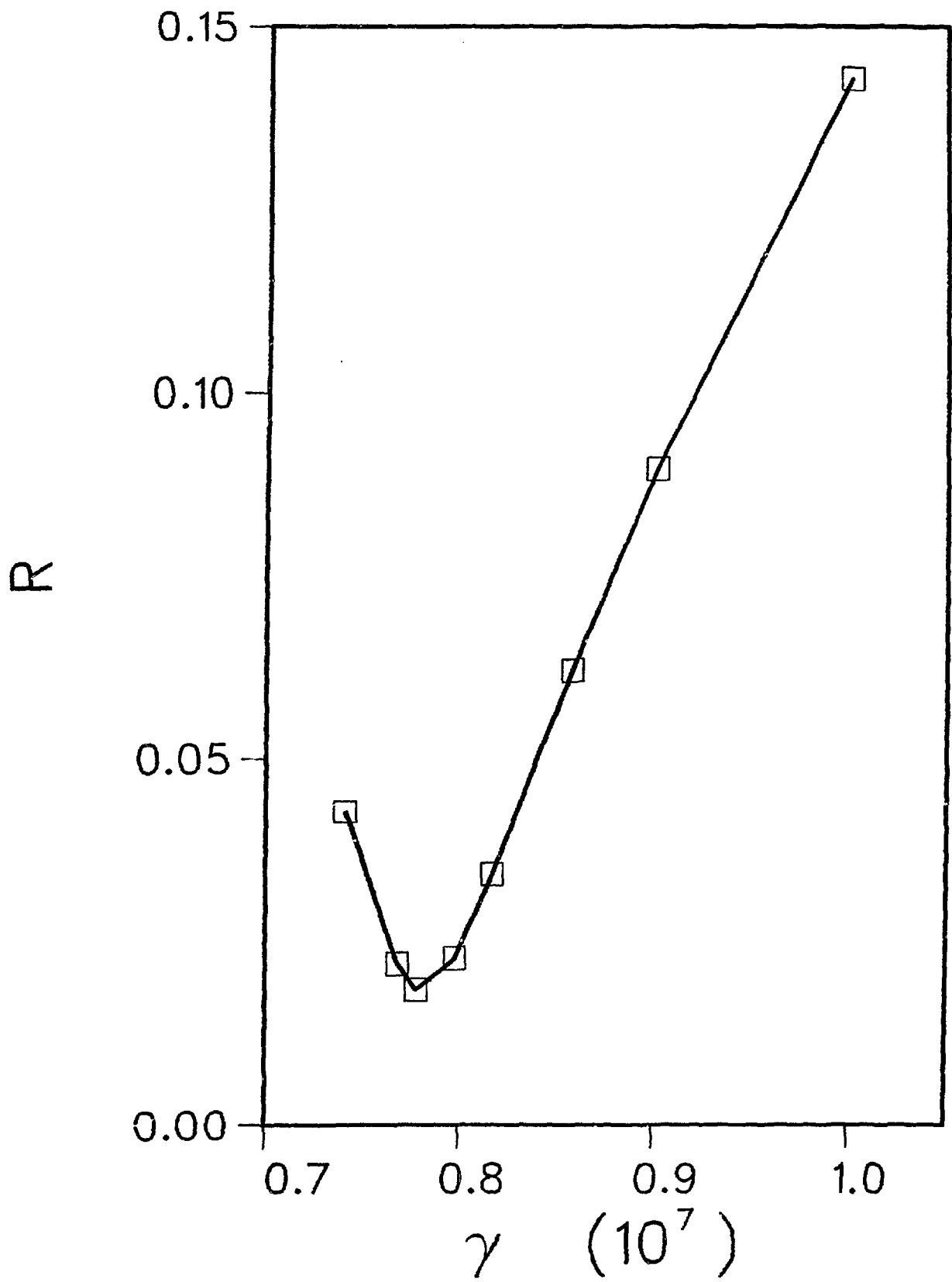


Figure 2

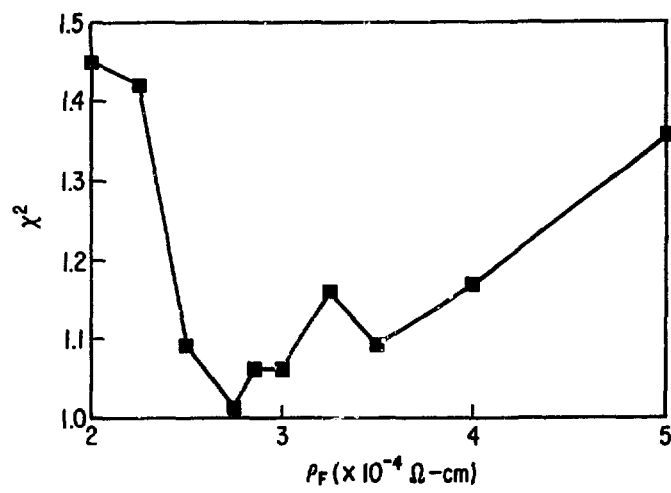


Figure 3

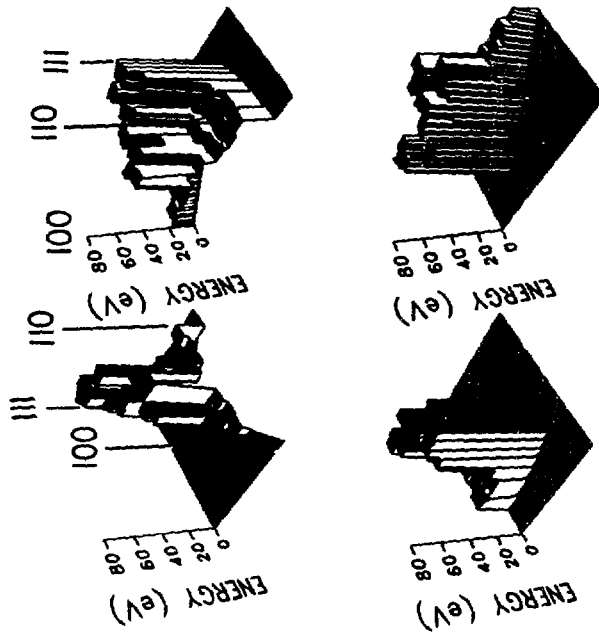


Figure 4b

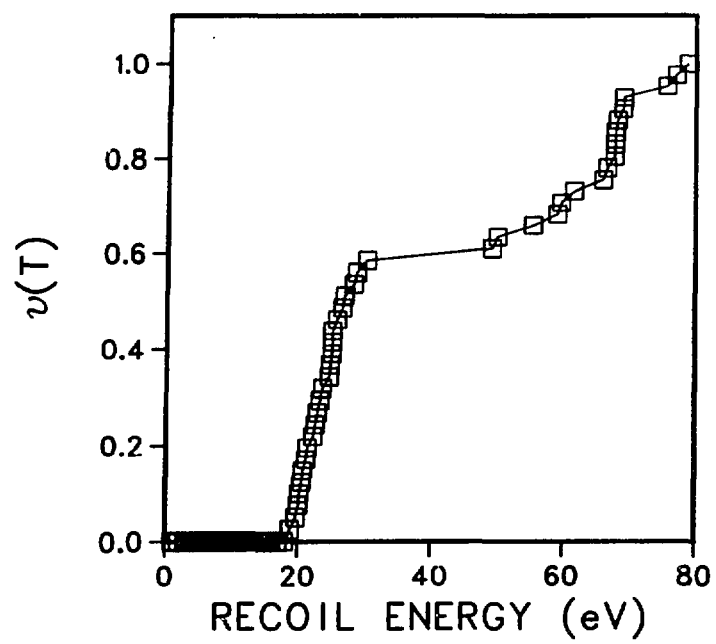


Figure 5

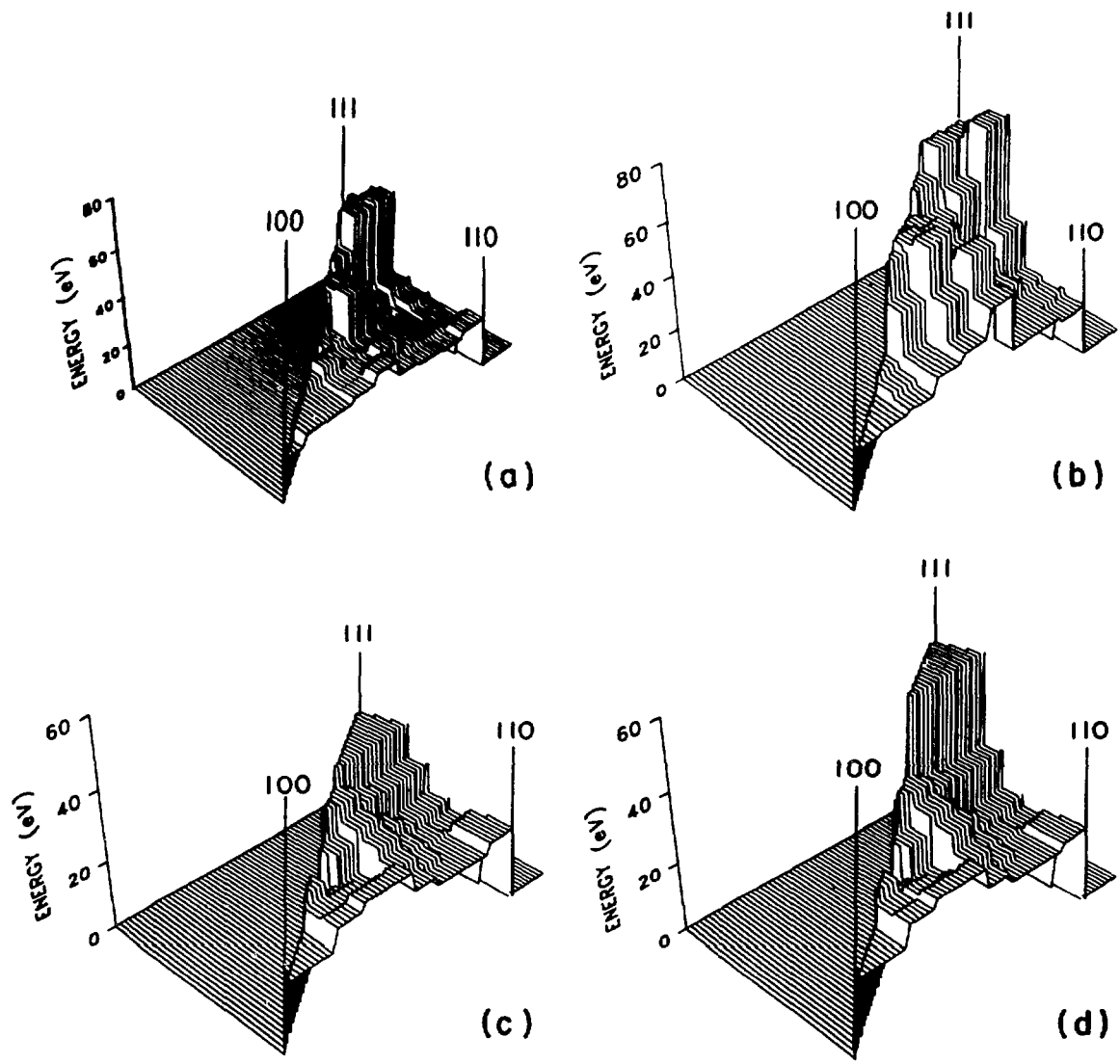


Figure 6

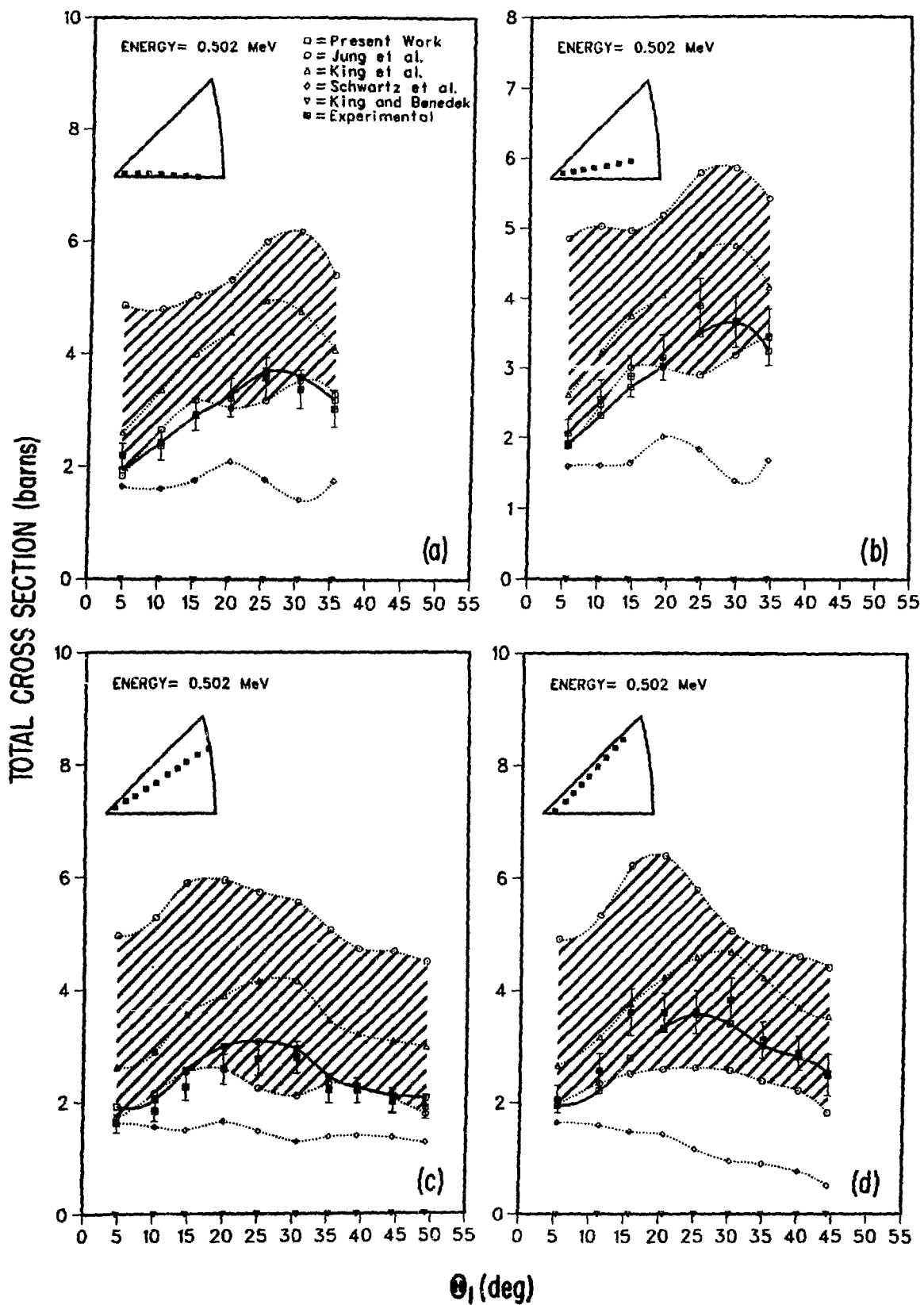


Figure 7

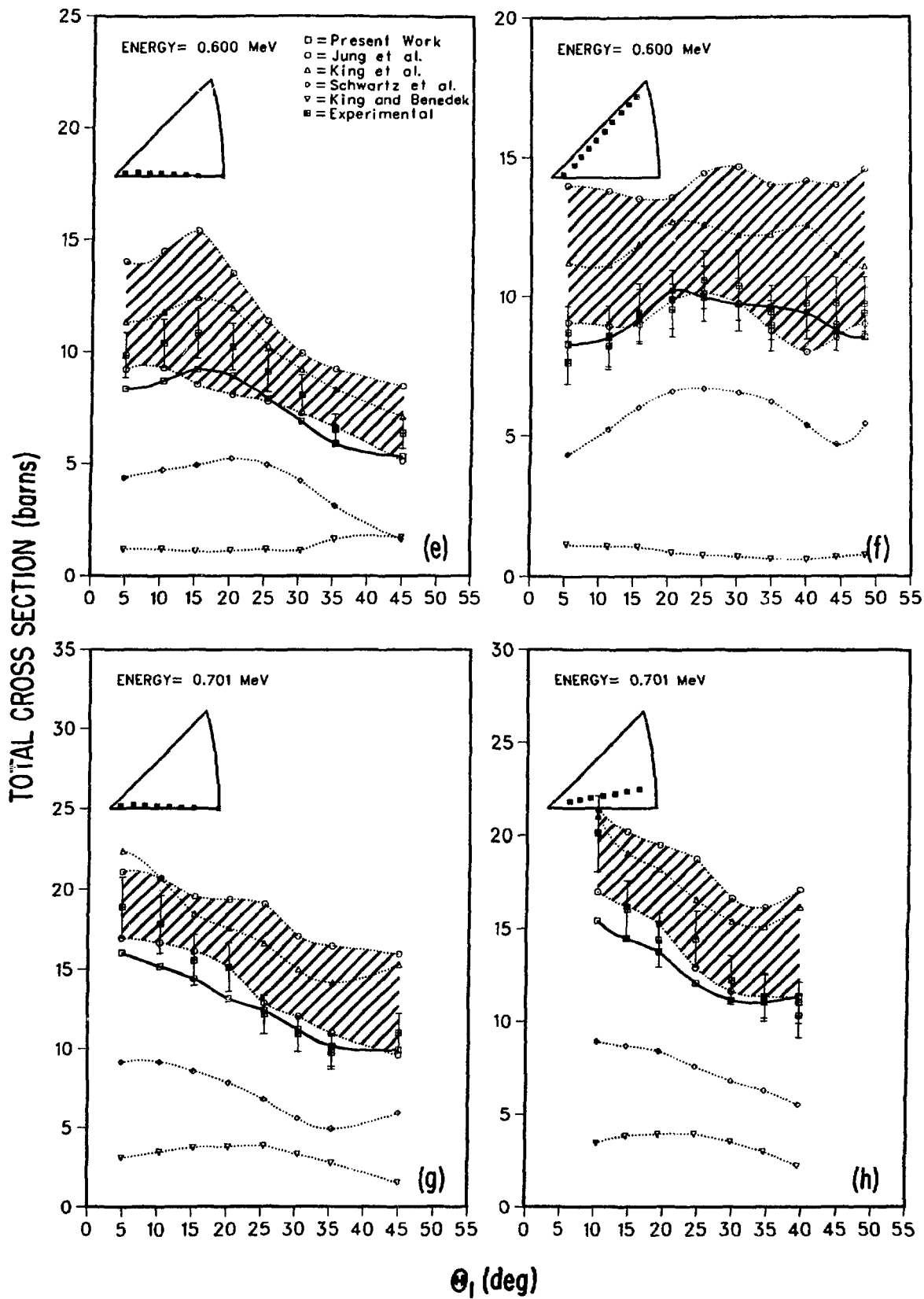


Figure 7

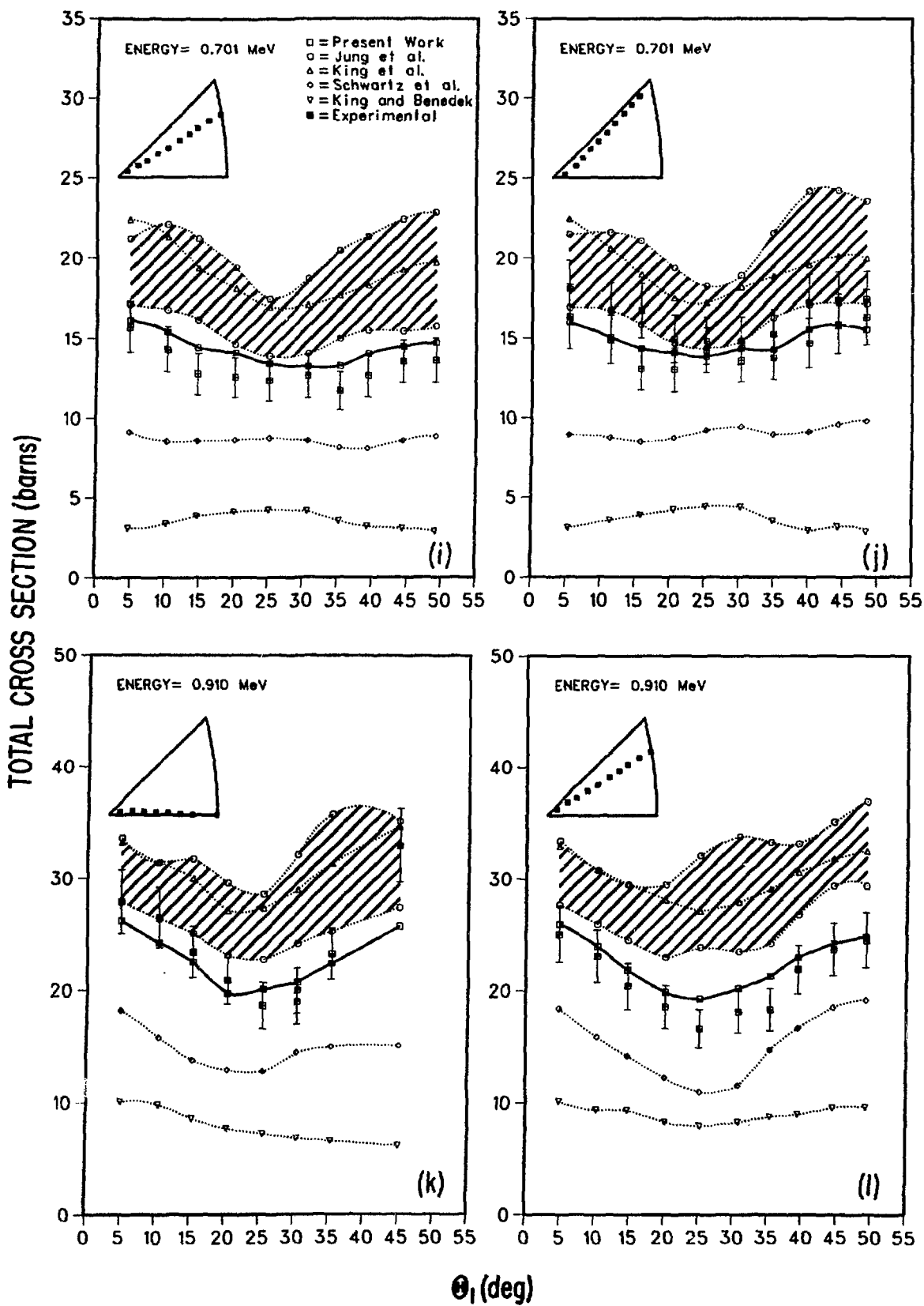


Figure 7

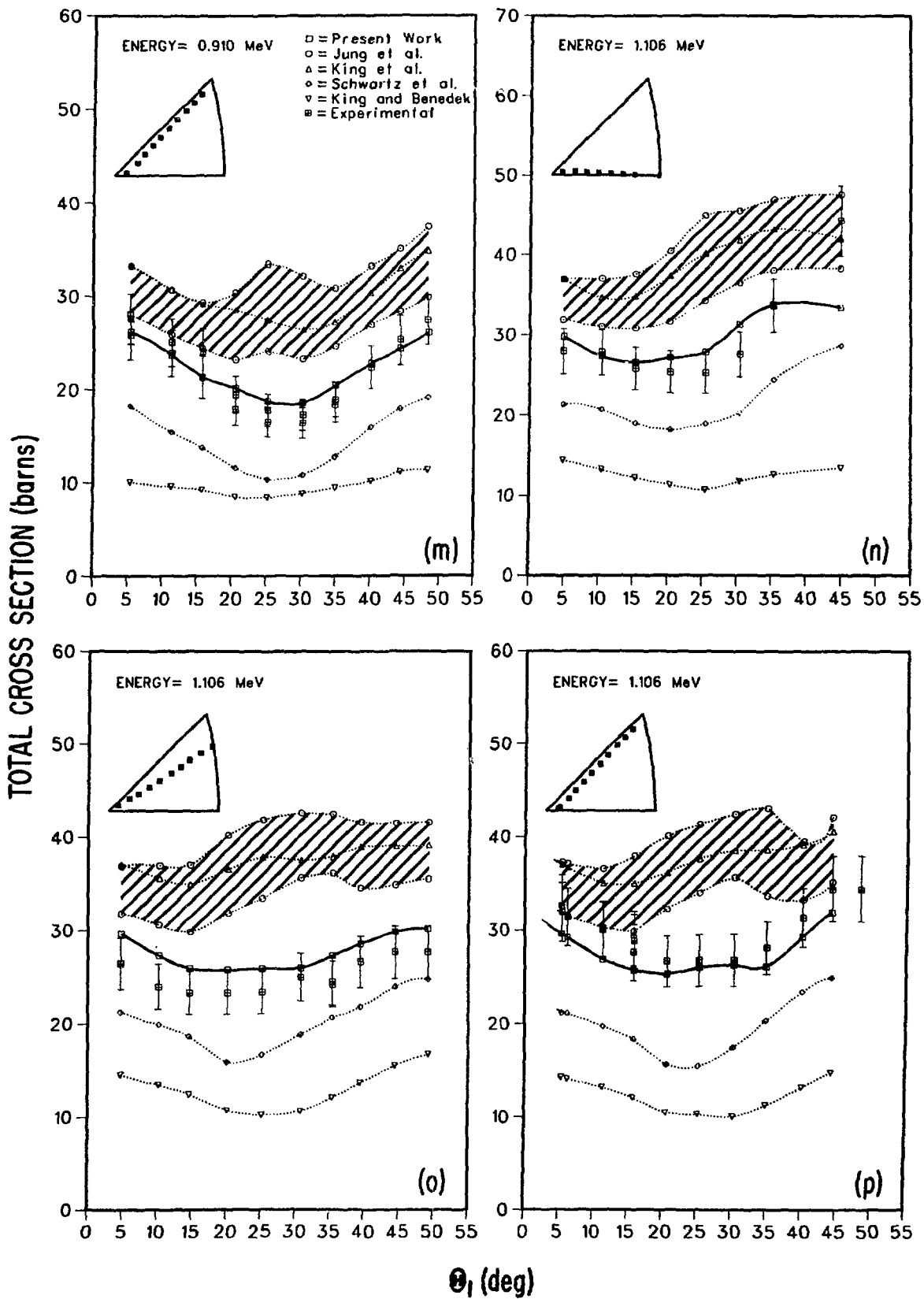


Figure 7

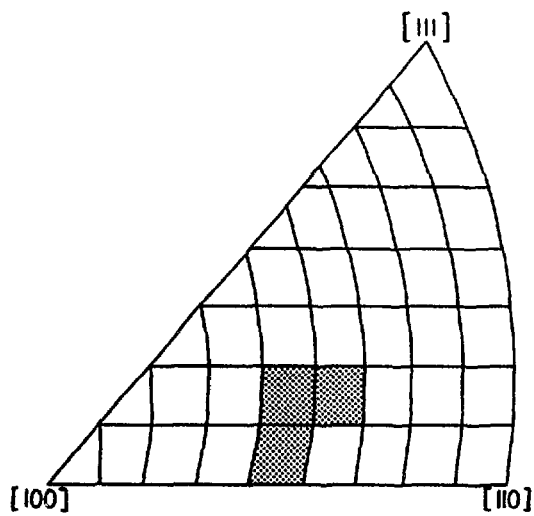


Figure 8a

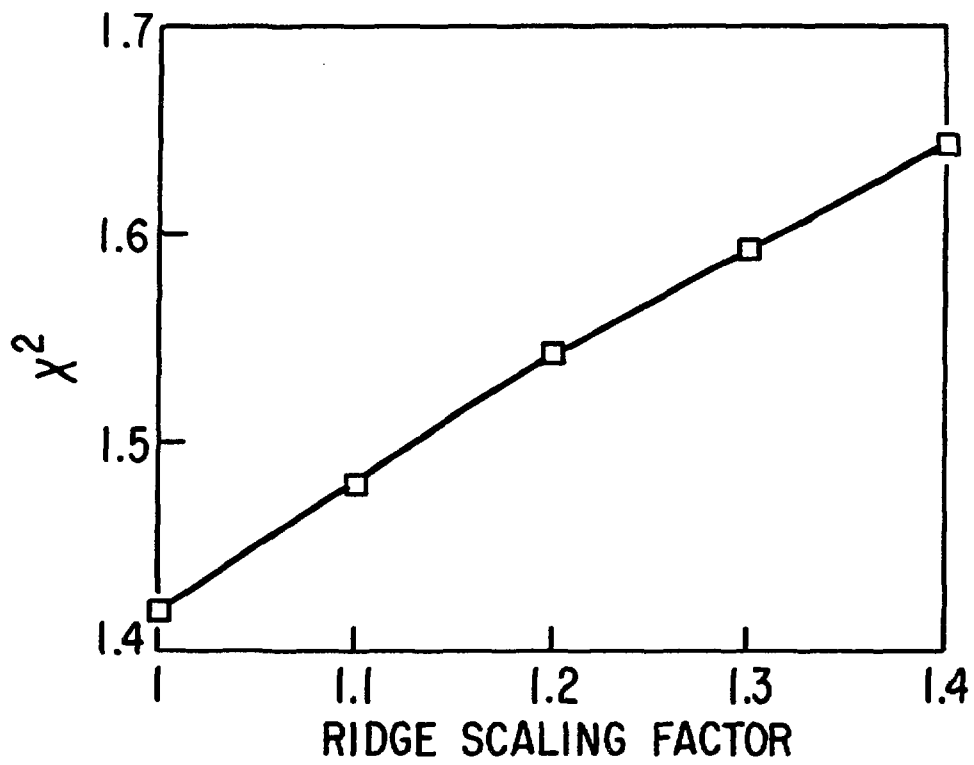


Figure 8b

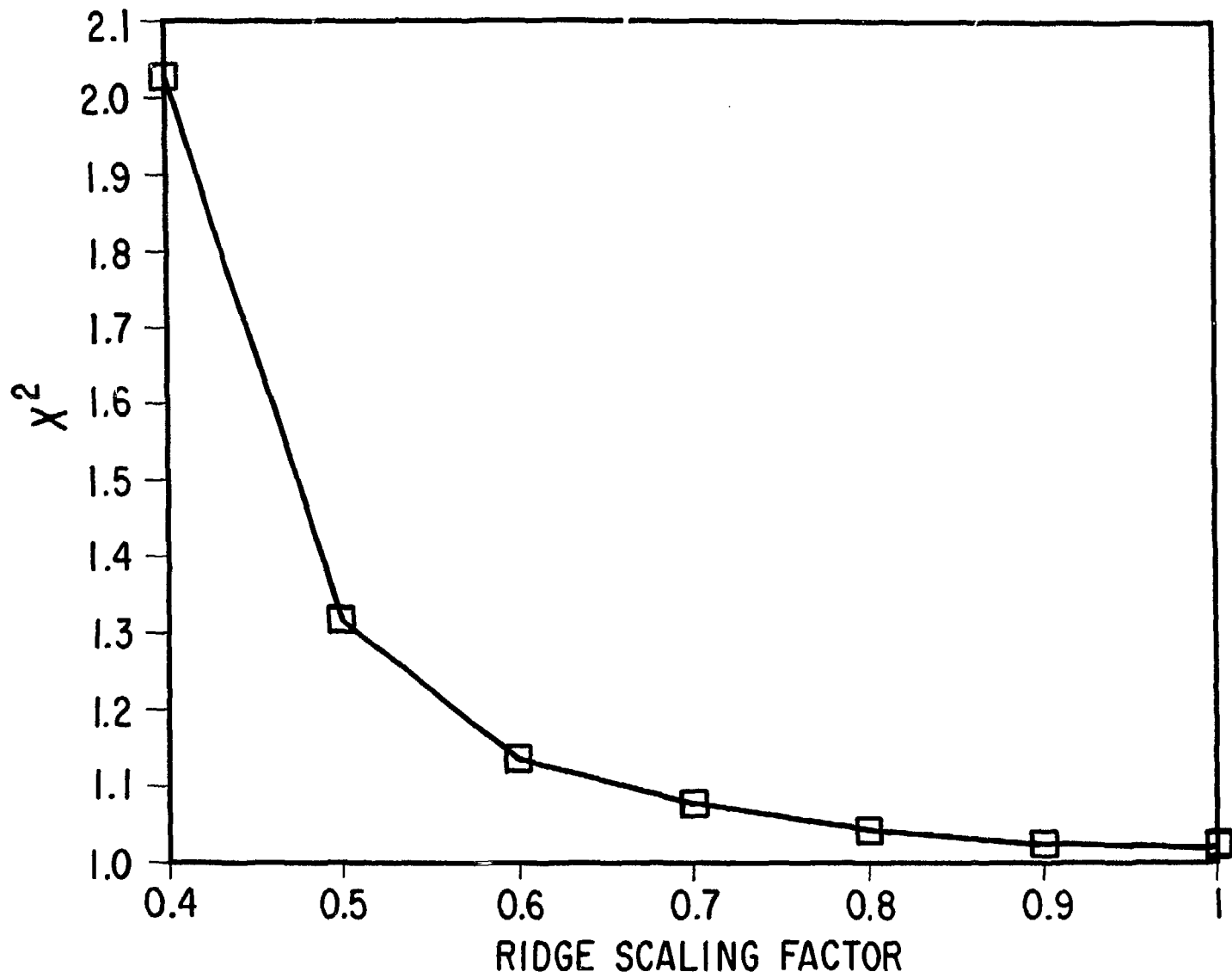


Figure 8c

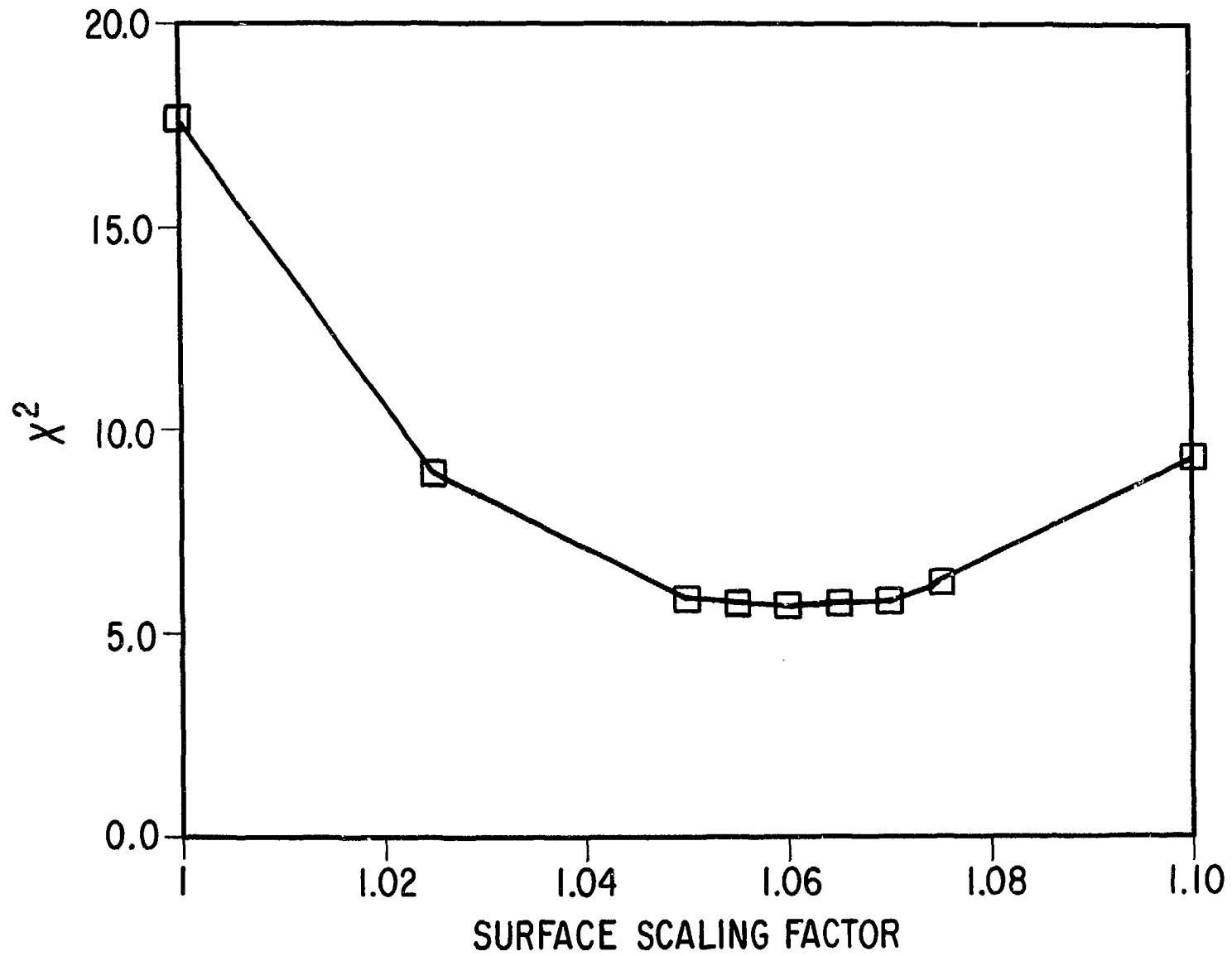


Figure 9